Available online at www.sciencedirect.com

SciVerse ScienceDirect

Ceramics International 38 (2012) 1281–1286

CERAMICS INTERNATIONAL

www.elsevier.com/locate/ceramint

AC transport properties of nanocrystalline SnO_2 semiconductor

P.P. Sahay [a,*], R.K. Mishra [a], S.N. Pandey [a], S. Jha [b], M. Shamsuddin [b]

[a] Department of Physics, Motilal Nehru National Institute of Technology, Allahabad 211 004, India
[b] Department of Metallurgical Engineering, Banaras Hindu University, Varanasi 221 005, India

Received 23 June 2011; received in revised form 15 August 2011; accepted 30 August 2011
Available online 6 September 2011

Abstract

Nanocrystalline SnO_2 materials were prepared by the chemical co-precipitation route by adding ammonia solution to 0.1 M solution of $SnCl_4{\cdot}5H_2O$. The resulting precipitate after thorough washing with distilled water and calcination at 600 °C for 10 h was investigated by XRD for phase identification and crystallite size determination. The materials have been found to be polycrystalline SnO_2, possessing tetragonal rutile crystal structure and nanocrystalline in grain size of approximately 30 nm. The TEM micrograph shows agglomerated particles (cluster of primary crystallites) with an average size of 37.4 nm. A corresponding selected area electron diffraction pattern reveals the different Debye rings of SnO_2, as analyzed in XRD.

The complex dielectric constant ε^* has been found to vary with frequency which is attributed to the multi-relaxation time constants of the energy states responsible for conduction mechanism. At any particular frequency, ε^* has been found to increase with temperature. The frequency dependence of loss tangent tan δ has been explained with the help of the equivalent circuit model. The observed frequency dependence of ac conductivity has been found to obey the power law: $\sigma_{ac} \propto \omega^S$, where variation of S with temperature indicates multi-hopping conduction mechanism in nanocrystalline SnO_2 samples. The complex impedance plots of Z' versus Z'' at different temperatures have been found to be single semicircular arcs with a non-zero intersection with the real axis in the high frequency region and have their centres lying below the real axis at a particular angle of depression, indicating multirelaxation processes in the material.

Keywords: SnO_2 nanoparticles; Complex dielectric constant; Loss tangent; AC conductivity; Impedance spectroscopy

1. Introduction

Tin dioxide (SnO_2) belongs to the family of an important *n*-type wide-bandgap semiconductors (E_g = 3.6 eV at 300 K). In its tetragonal rutile structure inherent oxygen vacancies act as an *n*-type dopant [1]. The unit cell parameters are a = 4.737 Å and c = 3.185 Å and its space group is $P42/mmm$. In recent years SnO_2 has attracted a lot of interests because of its wide range of applications as gas sensors [2–4], heat mirrors [5,6], transparent electrodes for solar cells [7], opto-electronic devices [8], etc. For various applications, this material has been exploited in the form of single crystals [9], compressed pellets [10], thin films [11] and thick films [12]. Very recently, nanocrystalline SnO_2 has gained prominence in technological field due to its interesting electrical and optical properties arising out of large surface-to-volume ratio, quantum confinement effect, etc. Starke et al. [13] have studied laser-ablated nanocrystalline SnO_2 material for low-level CO detection. Sensing characterization of NH_3 of nanocrystalline Sb-doped SnO_2 has been carried out by Wang et al. [14]. El-Etre et al. [15] have characterized nanocrystalline SnO_2 thin film for dye-sensitized solar cell application.

The optimization of device development based on SnO_2 material requires a better understanding of the transport properties of this material. Though a large number of studies on the dc conduction mechanism of SnO_2 have been carried out [16–19] but comparatively a little attention has been paid to the investigation of ac transport properties [20,21]. Dielectric measurements give an insight of the relaxation behaviour of the charge conduction species which, in turn, are responsible for the charge holding capacity, i.e., ac capacitance of the system. Ac conductivity measurements provide information about the interior of the materials in the region of low conductivity and are helpful in distinguishing the hopping conduction in the

* Corresponding author. Tel.: +91 532 2271260; fax: +91 532 2545341.
E-mail address: dr_ppsahay@rediffmail.com (P.P. Sahay).

0272-8842/$36.00
doi:10.1016/j.ceramint.2011.08.062

localized states from the free band conduction. Analysis of complex impedance spectra can be used to resolve the contribution of various processes such as bulk conduction, grain boundary conduction and transport across electrode–sample interface in the total conductivity of the polycrystalline system. In this paper we report a detailed study on the ac transport properties of SnO_2 nanoparticles.

To prepare active nanocrystalline powders, several chemical techniques have been investigated and reported in the literature. Among the various methods of preparing nanostructured SnO_2, co-precipitation [22], sol–gel [23], spray pyrolysis [24], hydrothermal routes [25], etc. are popular. In the present investigation, the authors have used co-precipitation method for the preparation of nanocrystalline SnO_2 materials as this method requires little manipulation and no sophisticated equipment.

2. Experimental

The nanocrystalline SnO_2 materials were prepared by the chemical co-precipitation route. The experimental details are as follows: all the chemicals used were of analytical grade. Firstly, stannic tetrachloride hydrated ($SnCl_4{\cdot}5H_2O$) was dissolved in distilled water to prepare 0.1 M solution. Ammonia solution was then added into the solution under constant agitation to form white slurry. The slurry was filtered and washed thoroughly with distilled water several times to remove the chloride ions completely from the precipitate. The resulting precipitate was dried at 90 °C and then calcined at 600 °C for 10 h in air. The dried mass was then crushed into fine powder. The structural analysis of the SnO_2 powder was carried out using PANalytical X'Pert Pro X-ray Diffractometer with CuKα radiation (λ = 1.5418 Å) as X-ray source at 40 kV and 30 mA in the scanning angle (2θ) from 20° to 80°. The morphologies and dimensions of the powders were observed by transmission electron microscopy (TEM), which were taken on a Philips model Tecnai-20 using an accelerating voltage of 200 kV.

For electrical measurements, the fine powder of SnO_2 was pressed into pellets of 12 mm diameter and 2.5 mm thickness at a pressure of ∼15 MPa using a hydraulic press. These pellets were sintered at around 600 °C for 5 h in air. The flat faces of the sintered pellets were polished and then coated with a thin layer of high temperature silver paste for making good electrical contacts. The pellet was then mounted on a home-made two-probe assembly which was inserted coaxially inside a resistance-heated furnace. The temperature of the pellets was monitored using a chromel–alumel thermocouple with the help of a Motwane digital multimeter (Model: 454). The ac measurements (impedance and phase angle) on the pellets were carried out as a function of frequency (100 Hz to 2 MHz) in the temperature range of 300–400 K by Precision Impedance Analyzer (Agilent Technologies; Model: 4294A). Throughout the measurements, the pellet in the furnace was allowed to equilibrate at each temperature for more than 10 min.

3. Results and discussion

3.1. Structural analysis

Fig. 1 shows the XRD pattern of the SnO_2 powder which matches with JCPDS File No. 72-1147. All the prominent peaks in the pattern have been found to correspond to the tetragonal rutile structure of polycrystalline SnO_2 and have been indexed on the basis of JCPDS file.

The lattice constants 'a' and 'c' for the tetragonal phase structure have been determined by the relation [26]:

$$\frac{1}{d^2} = \left(\frac{h^2 + k^2}{a^2}\right) + \left(\frac{1^2}{c^2}\right) \quad (1)$$

where 'd' is the interplaner spacing and ($h\,k\,l$) are miller indices, respectively. The lattice constants 'a' and 'c' thus calculated are 4.685 Å and 3.175 Å, respectively.

The average crystallite size (D) of the SnO_2 nanoparticles has been estimated for the three observed planes (1 1 0), (1 0 1) and (2 1 1) by using Scherrer formula [27]:

$$D = \frac{0.9\lambda}{\beta\cos\,\theta} \quad (2)$$

where λ, β and θ are the X-ray wavelength, full width at half maximum (FWHM) of the diffraction peak and the Bragg's diffraction angle, respectively. The crystallite size thus estimated has been found to be ∼30 nm.

The bright-field TEM image and the selected area electron diffraction (SAED) pattern of the synthesized SnO_2 nanoparticles are shown in Figs. 2 and 3, respectively. The TEM micrograph shows agglomerated particles (cluster of primary crystallites) with an average size of 37.4 nm which is close to the size calculated from XRD. The SAED pattern is consistent with the tetragonal rutile structure of SnO_2 featuring strong ring patterns assigned to (1 1 0), (1 0 1), (2 0 0), (2 1 1), (2 2 0), (0 0 2) and (3 1 0) planes and proves the high crystallinity of the nanoparticles.

The X-ray density (ρ_x), experimental density (ρ_a) and porosity (P) of the synthesized SnO_2 nanoparticle pellets have

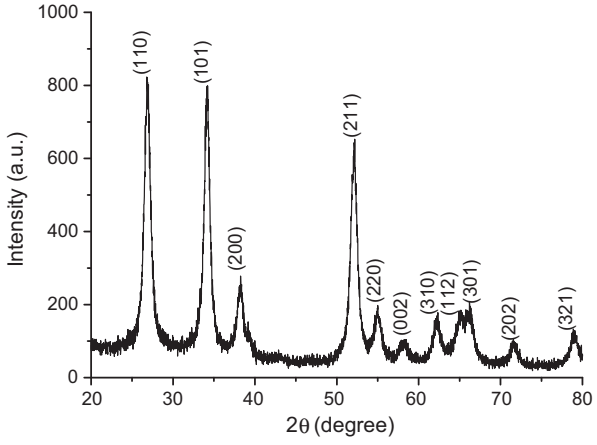

Fig. 1. XRD spectra of the SnO_2 nanoparticles.

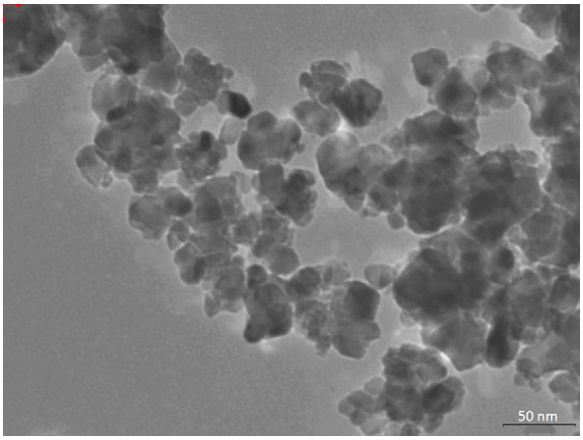

Fig. 2. TEM micrograph of the SnO_2 nanoparticles.

been calculated as follows [28].

$$\rho_x = \frac{nM}{Na^2c} \tag{3}$$

$$\rho_a = \frac{m}{v} = \frac{m}{\pi r^2 h} \tag{4}$$

$$P = \left(1 - \frac{\rho_a}{\rho_x}\right) \times 100\% \tag{5}$$

Here n is the number of molecules per unit cell, M is the molecular weight, a and c are the lattice parameters, N is the Avogadro's number while m, v, r, and h are the mass, volume, radius, and thickness of the cylindrical pellet, respectively. The porosity thus calculated has been found to be 52.9%.

3.2. Dielectric relaxation

The complex dielectric constant ε^* of a material is represented by two parts: $\varepsilon^* = \varepsilon' + \varepsilon''$, where ε' is the real part (dielectric constant) and ε'' the imaginary part (dielectric loss). The ratio between ε' and ε'' defines a loss tangent, $\tan\delta = \varepsilon''/\varepsilon'$.

The frequency dependence of ε^* of the nanocrystalline SnO_2 at different temperatures is shown in Fig. 4. At any particular frequency, ε^* has been found to increase with temperature. This means that the charge holding capacity of the energy states increases with temperature. This may be due to enhancement in the capture cross-section and/or the relaxation time of these states with rise in temperature. These energy states are created in the grain boundary structure because of the smaller grain size in the nanocrystalline material. Variation of ε^* with frequency is attributed to the multi-relaxation time constants of the energy states. As evident from the figure, the influence of energy states on ε^* begins to decrease at high frequencies because of their large relaxation time.

Loss tangent $\tan\delta$ represents the power dissipation in the samples. Fig. 5 presents the variation of $\tan\delta$ with frequency at different temperatures. The figure shows a decrease in $\tan\delta$ at low frequencies followed by a loss minimum and again an increase in $\tan\delta$ at high frequencies. The observed frequency dependence of $\tan\delta$ has been found consistent with that predicted by the equivalent circuit model of Goswami and Goswami [29] which comprises a capacitive element C in parallel with a resistive element R, both elements in series with a low value resistance R_1. Considering the equivalent circuit

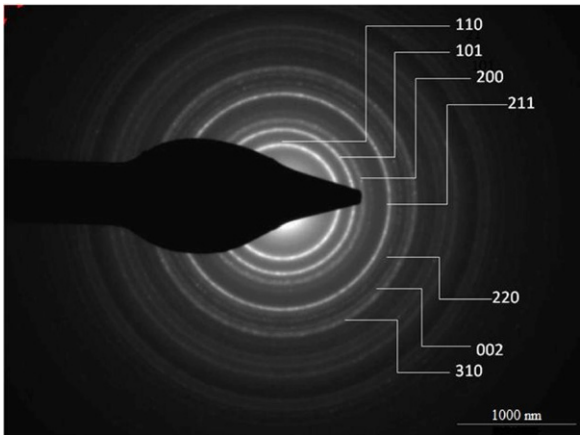

Fig. 3. SAED pattern of the SnO_2 nanoparticle.

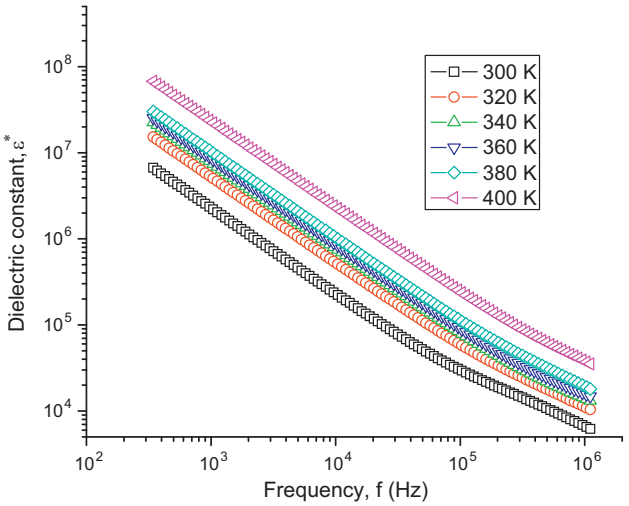

Fig. 4. Variation of ε^* with frequency at different temperatures.

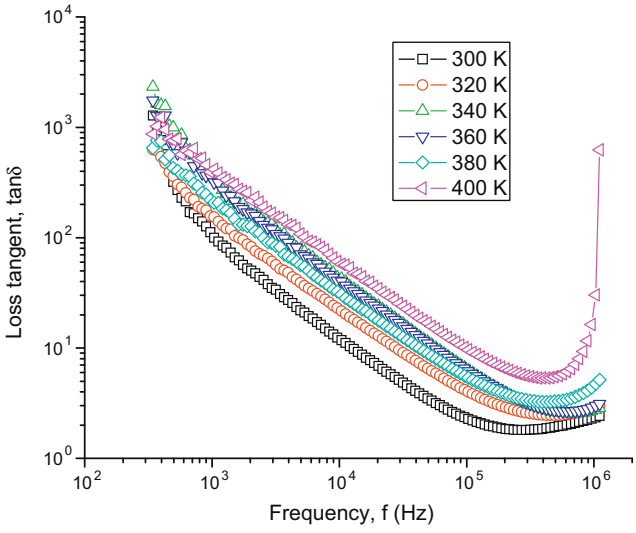

Fig. 5. Variation of $\tan\delta$ with frequency at different temperatures.

model shown in Fig. 6, the loss tangent is given by

$$\tan\ \delta = \left(\frac{1 + R_1/R}{\omega CR}\right) + \omega CR \tag{6}$$

In this equation, at low frequencies the term ω^{-1} is dominant and at high frequencies the term ω is dominant.

3.3. AC electrical conductivity

The ac conductivity of a material is represented by two parts: $\sigma_{ac}(\omega) = \sigma_1(\omega) + \sigma_2(\omega)$, where $\sigma_1(\omega)$ is the real part ($=2\pi f\varepsilon_0\varepsilon''$) and $\sigma_2(\omega)$ is the imaginary part ($=2\pi f\varepsilon_0\varepsilon'$).

Fig. 7 presents the ac conductivity of the nanocrystalline SnO_2 sample as a function of frequency at different temperatures. The frequency dependence of ac conductivity obeys the power law relation: $\sigma_{ac}(\omega) = A\omega^S$, where A is a complex proportionality constant and ω is the angular frequency. The exponent S is a frequency dependent parameter having value less than unity and its dependence on temperature determines the conduction mechanism in materials. In the correlated barrier hopping (CBH) model, S decreases with temperature [30]; whereas for the small polaron quantum mechanical tunneling model, S increases with temperature [31].

As depicted in Fig. 7, at all temperatures in the low frequency region, the ac conductivity is almost independent of frequency up to 10 KHz, and after that it shows significant frequency dependence. At lower temperatures the conductivity is strongly frequency dependent. Fig. 8 shows variation of S with temperature, which indicates multi-hopping conduction mechanism in nanocrystalline SnO_2 samples.

Fig. 9 presents the variation of ac conductivity with inverse absolute temperature at four different frequencies. It is observed that the conductivity increases with increasing temperature at all frequencies. This may be due to thermally assisted hoping conduction of charge carriers between different localized states. Fig. 9 shows the presence of two linear regions with different slopes. The slope change occurs at around 380 K. The activation energies calculated from the Arrhenius plots (Fig. 9) for two different temperature regions, are listed in Table 1. It is observed that as the frequency increases, the activation energy decreases. This may be due to the large lattice vibration at high frequencies which causes more conduction [32].

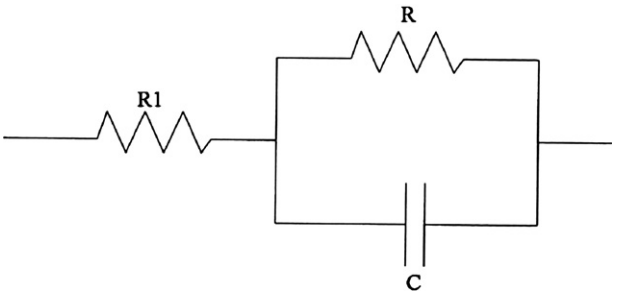

Fig. 6. Equivalent circuit model.

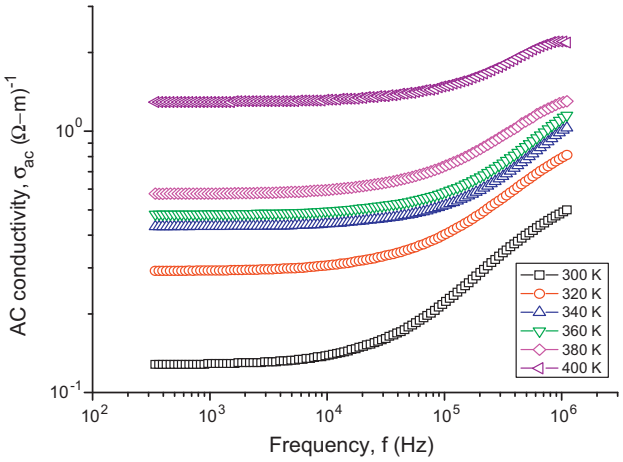

Fig. 7. Frequency dependence of ac conductivity at different temperatures.

3.4. Complex ac impedance

At any particular frequency, the complex ac impedance, Z^*, is expressed in terms of its real and imaginary components, Z' and Z'', by the relation $Z^* = Z' - jZ''$. The complex ac impedance, Z^*, may be transformed to one of the other three impedance formalisms: admittance, Y^*, relative permittivity, ε^*, and relative electric modulus, M^*, using the equations [33]:

$$Y^* = \frac{1}{Z^*} \tag{7}$$

$$e^* = \frac{1}{M^*} \tag{8}$$

$$M^* = j\omega C_0 Z^* \tag{9}$$

$$e^* = \frac{Y^*}{j\omega C_0} \tag{10}$$

where C_0 is the vacuum capacitance of the sample holder between electrodes having air gap in place of sample and

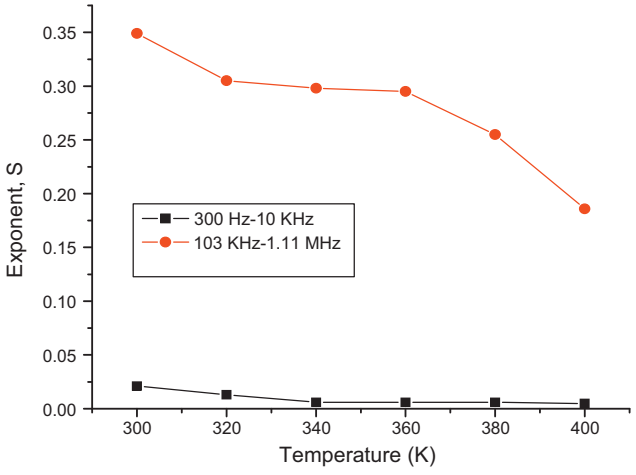

Fig. 8. Variation of exponent S with temperatures.

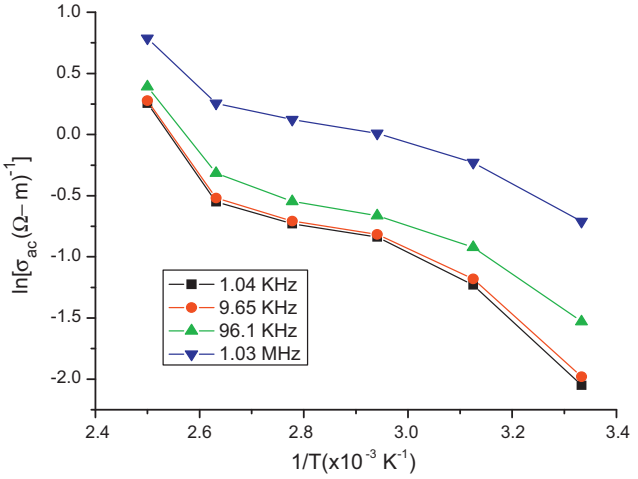

Fig. 9. Variation of ac conductivity with inverse absolute temperature at different frequencies.

defined as

$$C_0 = \varepsilon_0 \left(\frac{A}{t}\right) \tag{11}$$

Here ε_0 is the permittivity of the free space (8.85×10^{-14} F/cm), and A and t are the cross-sectional area and thickness of the sample.

Fig. 10(a) and (b) shows variation of Z^* and the phase angle θ as a function of frequency. The general features of the plots are similar to that observed for an RC circuit in parallel, where the impedance varies with the inverse of frequency. As depicted in Fig. 10(b), the phase angle initially increases with frequency up to certain range (for example, 315 KHz, in case of temperature 300 K) and afterwards begins to decrease with frequency. This indicates that the capacitive component of the RC circuit becomes less dominant at higher frequency region. It is observed that the phase angle variation is maximum at 300 K and decreases with rise in temperature. This implies that at higher temperatures, the influence of capacitive component decreases.

Fig. 11 shows variation of Z'' with frequency at different temperatures. These plots are found to exhibit Debye peaks at different temperatures. The peak maxima shift to the high frequency side with increasing temperature. The angular frequencies ω of the peak maxima are given by the reciprocal of the relaxation time, i.e., $\omega_m = 1/\tau = 1/(RC)$. Since the value of R decreases with rise in temperature, therefore ω_m is an increasing function of temperature. Similar results have also been reported by the authors in the case of sintered ZnO pellets [34].

Table 1
Activation energies calculated from the Arrhenius plots (Fig. 9).

Frequency (KHz)	Activation energy (eV)	
	300–380 K	380–400 K
1.04 KHz	0.176	0.528
9.65 KHz	0.171	0.522
96.1 KHz	0.14	0.464
1.03 MHz	0.114	0.349

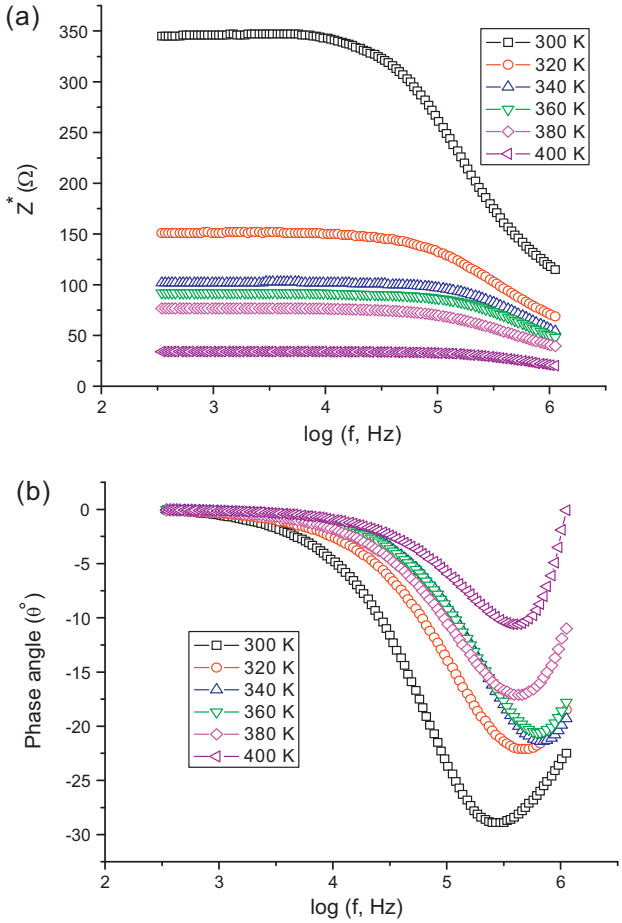

Fig. 10. (a) Frequency dependence of Z^* at different temperatures. (b) Frequency dependence of the phase angle θ at different temperatures.

Fig. 12 represents the complex impedance plots (Nyquist plots) of Z' versus Z'' at different temperatures. These plots are single semicircular arcs with their centres lying below the real axis at a particular angle of depression and have a non-zero intersection with the real axis in the high frequency region. A single semicircular arc observed in complex impedance plots suggests an electrical equivalent circuit composed of a resistance R and a capacitance C connected in parallel (Fig. 6). The addition

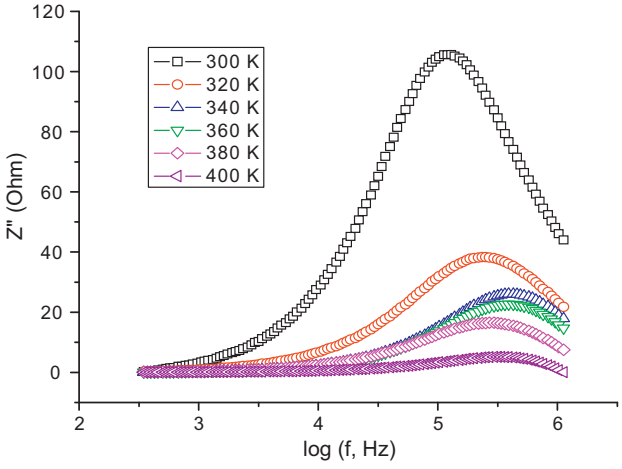

Fig. 11. Plots of Z'' versus frequency at different temperatures.

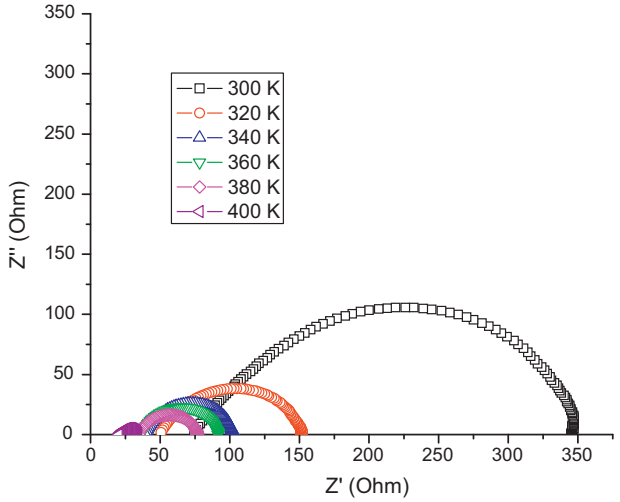

Fig. 12. Complex impedance plots of Z' versus Z'' at different temperatures.

of a series resistance R_1 (which is attributed to the core of the grains) shifts the circular arc from the origin. It is observed that the size of the plots shrink with the increase of temperature. Reduction in size of the plots is attributed to decrease in the value of R with rise in temperatures. Generally, the grain boundaries are effective in low frequency region while the grains are effective in high frequency region. Thus, the semicircular arc appearing in the low frequency region corresponds to the grain boundary contribution. Bose et al. [35] have investigated the room temperature complex impedance spectra of nanocrystalline SnO_2 samples and observed the impedance spectra as depressed single semicircular arcs.

4. Conclusion

(i) Nanocrystalline SnO_2 materials prepared by the chemical co-precipitation route have been found to possess tetragonal rutile structure, having crystallite size of approximately 30 nm. The SAED pattern reveals the different Debye rings of SnO_2, as analyzed in XRD.
(ii) At any particular frequency, ε^* has been found to increase with temperature. This may be due to enhancement in the capture cross-section and/or the relaxation time of the energy states with rise in temperature.
(iii) The frequency dependence of ac conductivity has been found to obey the power law relation: $\sigma_{ac}(\omega) = A\omega^S$, where variation of S with temperatures indicates multi-hopping conduction mechanism in nanocrystalline SnO_2 samples.
(iv) Impedance spectroscopy studies show single semicircular arcs in the complex impedance spectra at all temperatures, with their centres lying below the real axis at a particular angle of depression, indicating multirelaxation processes in the material.

Acknowledgements

Authors are grateful to the Head, Department of Metallurgical Engineering, Banaras Hindu University, Varanasi, India for providing experimental facilities for ac measurements. They are also thankful to the Head, Department of Metallurgical Engineering & Material Science, Indian Institute of Technology Bombay, India for providing XRD facilities, and the Director, Sophisticated Instrumentation Centre for Applied Research & Testing, Vallabh Vidya Nagar, Anand, India for TEM characterization. The financial support provided by the Department of Science & Technology, Govt. of India, in the form of a research project (No. SR/S2/CMP-41/2008) is gratefully acknowledged.

References

[1] Z. Chen, J.K.L. Lai, C.-H. Shek, H. Chen, J. Mater. Res. 18 (2003) 1289.
[2] F. Hellegouarc'h, F. Arefi-Khonsari, R. Planade, J. Amouroux, Sens. Actuators B 73 (2001) 27.
[3] Z. Jiao, X. Wan, B. Zhao, H. Guo, T. Liu, M. Wu, Bull. Mater. Sci. 31 (2008) 83.
[4] Y. Shimizu, T. Maekawa, Y. Nakamura, M. Egashira, Sens. Actuators B 46 (1998) 163.
[5] M. Kojima, F. Takahashi, K. Kinoshita, T. Nishibe, M. Ichidate, Thin Solid Films 392 (2001) 349.
[6] C. Choudhury, H.K. Sehgal, Energy Convers. Manage. 29 (1989) 265.
[7] J.H. Lee, N.G. Park, Y.J. Shin, Sol. Energy Mater. Sol. Cells 95 (2011) 179.
[8] C.G. Granqvist, Sol. Energy Mater. Sol. Cells 91 (2007) 1529.
[9] Y. Liang, J. Fan, X. Xia, Z. Jia, Mater. Lett. 61 (2007) 4370.
[10] C. Bulpitt, S.C. Tsang, Sens. Actuators B 69 (2000) 100.
[11] T. Ohgaki, R. Matsuoka, K. Watanabe, K. Matsumoto, Y. Adachi, I. Sakaguchi, S. Hishita, N. Ohashi, H. Haneda, Sens. Actuators B 150 (2010) 99.
[12] K. Jain, R.P. Pant, S.T. Lakshmikumar, Sens. Actuators B 113 (2006) 823.
[13] T.K.H. Starke, G.S.V. Coles, Sens. Actuators B 88 (2003) 227.
[14] Y. Wang, Q. Mu, G. Wang, Z. Zhou, Sens. Actuators B 145 (2010) 847.
[15] A.Y. El-Etre, S.M. Reda, Appl. Surf. Sci. 256 (2010) 6601.
[16] J. Ni, X. Zhao, X. Zheng, J. Zhao, B. Liu, Acta Mater. 57 (2009) 278.
[17] A.V. Gaponov, A.B. Glot, J. Mater. Sci.: Mater. Electron. 21 (2010) 331.
[18] A.B. Glot, A.V. Gaponov, A.P. Sandoval-García, Physica B 405 (2010) 705.
[19] F. Hernandez-Ramirez, A. Tarancon, O. Casals, E. Pellicer, J. Rodriguez, A. Romano-Rodriguez, J.R. Morante, S. Barth, S. Mathur, Phys. Rev. B 76 (2007) 085429.
[20] P.R. Bueno, S.A. Pianaro, E.C. Pereira, L.O.S. Bulhoes, E. Longo, J.A. Varela, J. Appl. Phys. 84 (1998) 3700.
[21] L.L. Diaz-Flores, R. Ramirez-Bon, A. Mendoza-Galvan, E. Prokhorov, J. Gonzalez-Hernandez, J. Phys. Chem. Solids 64 (2003) 1037.
[22] A. Chandra Bose, D. Kalpana, P. Thangadurai, S. Ramasamy, J. Power Sources 107 (2002) 138.
[23] O.K. Varghese, L.K. Malhotra, G.L. Sharma, Sens. Actuators B 55 (1999) 161.
[24] R.R. Kasar, N.G. Deshpande, Y.G. Gudage, J.C. Vyas, R. Sharma, Physica B 403 (2008) 3724.
[25] H. Zhu, D. Yang, G. Yu, H. Zhang, K. Yao, Nanotechnology 17 (2006) 2386.
[26] B.D. Cullity, Elements of X-ray Diffraction, Addison-Wesley, New York, 1978.
[27] H.P. Klug, L.E. Alexander, X-Ray Diffraction Procedures for Polycrystalline and Amorphous Materials, Wiley, New York, 1974.
[28] M. Abdullah Dar, K. Mujasam Batoo, V. Verma, W.A. Siddiqui, R.K. Kotnala, J. Alloys Compd. 493 (2010) 553.
[29] A. Goswami, A.P. Goswami, Thin Solid Films 16 (1973) 175.
[30] P.N. Butcher, P.L. Morys, J. Phys. C: Solid State Phys. 6 (1973) 2147.
[31] L.J. Meng, Y.M. Adritsck, M.P. Dos Santos, Vacuum 45 (1994) 19.
[32] A. Abdel-All, J. Mater. Sci. Technol. 14 (1998) 247.
[33] E.J. Abram, D.C. Sinclair, A.R. West, J. Electroceram. 10 (2003) 165.
[34] P.P. Sahay, S. Tewari, R.K. Nath, S. Jha, M. Shamsuddin, J. Mater. Sci. 43 (2008) 4534.
[35] A. Chandra Bose, P. Balaya, P. Thangadurai, S. Ramasamy, J. Phys. Chem. Solids 64 (2003) 659.